Effect of covalent bonding on the superconducting critical temperature of the H-S-Se system

Binbin Liu,[1] Wenwen Cui,[1,*] Jingming Shi,[1] Li Zhu,[2] Ju Chen,[1] Shuyi Lin,[1] Ruiming Su,[1] Jiayu Ma,[1] Kang Yang,[1] Meiling Xu,[1] Jian Hao,[1] Artur P. Durajski,[3] Jingshan Qi,[1] Yanling Li,[1] and Yinwei Li[1,†]

[1]*School of Physics and Electronic Engineering, Jiangsu Normal University, Xuzhou 221116, China*

[2]*Extreme Materials Initiative, Geophysical Laboratory, Carnegie Institution of Washington, 5251 Broad Branch Road, NW, Washington, D.C. 20015, USA*

[3]*Institute of Physics, Częstochowa University of Technology, Aleja Armii Krajowej 19, 42-200 Częstochowa, Poland*

Hydrogen-rich materials have attracted great interest since the recent discovery of superconductivity at 203 K in highly compressed hydrogen sulfide. To probe the role of covalent bonding in determining the T_c of hydrogen-related superconductors, we systematically studied the crystal structure and superconductivity of H_6SSe, a hypothetical compound derived from H_3S with half its S atoms replaced by group neighbor Se. First-principles structure searches identify three dynamically stable structures for H_6SSe at 200 GPa. Interestingly, all three structures keep the main feature of the cubic $Im\bar{3}m$ structure of H_3S, but with different Se substitution positions. Electron-phonon coupling calculations reveal the superconductive potential of the three phases of H_6SSe, with T_c decreasing (from 195 to 115 K) upon the declining strength of the weakest covalent H-S or H-Se bonds in each structure, thereby highlighting the key role of covalent bonding in determining T_c. For comparison, O-substituted H_6SO was predicted to assume a semiconducting phase with entirely different structural features from H_6SSe. We attribute this difference to the much stronger electronegativity of O (3.44) compared with S (2.58) or Se (2.55).

I. INTRODUCTION

Since Onnes's first observation of superconductivity in 1911 [1], research on the topic has followed two main branches: the search for new superconductors with high critical temperatures T_c and exploration of the superconducting mechanism. BCS theory [2] is a particularly successful description of conventional superconductors and has aided the design of high-T_c superconductors. According to BCS theory, a high-T_c superconductor satisfies three conditions: large electron density of states at the Fermi level, high phonon frequencies, and strong electron-phonon coupling. Ashcroft suggested solid hydrogen (H_2) as the perfect candidate [3]; however, metalizing H_2 remains a challenge, with a recent report claiming its synthesis at 495 GPa [4]. Hydrogen-rich compounds have also been suggested to be suitable substitutes for pure hydrogen that can be metalized at much lower pressure [5], and many theoretical studies have proposed good superconductor candidates, e.g., group-IVA hydrides (SiH_4 [6–9], Si_2H_6 [10,11], GeH_4 [12], and $SiH_4(H_2)_2$ [13,14]), group-VA hydrides (PH [15], PH_2 [15,16], PH_3 [17], AsH_8, and SbH_4 [18]), and "cagelike" hydrides (CaH_6 [19], YH_6 [20], LaH_{10}, and YH_{10} [21,22]).

Solid H_2S was not initially considered a promising superconducting hydride because it is believed to dissociate into its constituent elements under high pressure before metalization. A breakthrough in 2015 by Drozdov *et al.* [23] found a record-high T_c of 203 K for H_2S highly compressed at 153 GPa. This discovery was inspired by our previous theoretical prediction that H_2S is stable against dissociation, although with superconductivity at around 80 K and 160 GPa [24]. The superconducting state of compressed H_2S was again confirmed by the expulsion of magnetic field via nuclear resonant scattering [25]. H_2S shows two different superconductivity states at high pressure: a low-T_c (33–150 K) or high-T_c (203 K) phase emerges depending on whether the H_2S is prepared at low (100 K) or high (200–300 K) temperature, respectively. Many theoretical and experimental works [24,26–38] have reached a consensus that these phases respectively comprise the original sample H_2S and its decomposition product H_3S. Note that H_3S was first synthesized in 2011 by Strobel *et al.* [39] and was subsequently predicted to be a superconductor at high pressure by Duan *et al.* [27]. Significantly, the T_c of the cubic $Im\bar{3}m$ structure of H_3S was predicted to be as high as ~200 K at 200 GPa, very close to that of the high-T_c phase of compressed H_2S, which led to speculation that H_2S decomposes into H_3S at high pressure. A recent optical spectroscopy study provided direct evidence that H_3S is a conventional superconductor whose superconductivity originates from electron-phonon interactions [34].

The mechanism of the high T_c of $Im\bar{3}m$ H_3S has become a hot topic, as it could aid the pursuit of new high-T_c superconductors. The T_c value can be affected by several factors such as the strong anharmonic effect [26], quantum hydrogen-bond symmetrization [34], the exchange-correlation approximation used [40], and the Van Hove singularities around the Fermi level [41,42]. Moreover, it was suggested that the strong H-S covalent bonding in the metallic state plays a key role in the
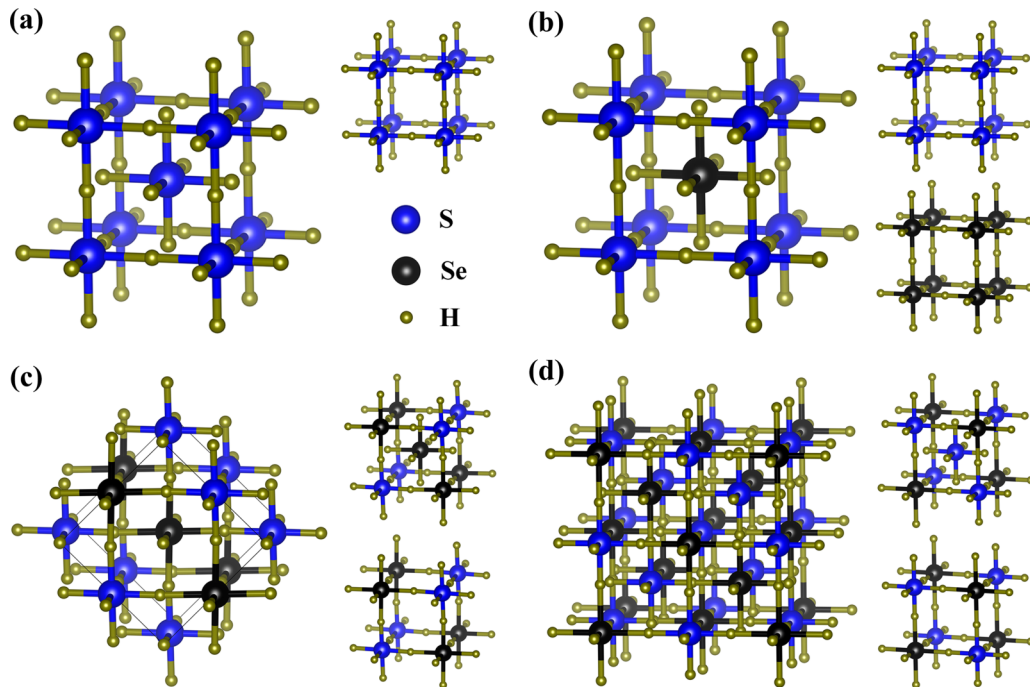
*wenwencui@jsnu.edu.cn
†yinwei_li@jsnu.edu.cn

FIG. 1. (a) The $Im\bar{3}m$ structure of H_3S and (b)–(d) the predicted $Pm\bar{3}m$, $Cmmm$, and $Fd\bar{3}m$ structures of H_6SSe at 200 GPa, respectively. The right panels represent their building sublattices.

large electron-phonon coupling [36], which is similar to that in MgB_2. The effect of bonding on the superconductivity of H_3S was previously explored by replacing S atoms with mixtures of chalcogens (O, S, Se, and Te) and other atoms [43]. T_c was enhanced by the partial doping of more electronegative species, e.g., O (to give $H_3O_{0.5}S_{0.5}$) and halogens [43]. Ge *et al.* investigated the effects of group-VA, -VIA, and -VIIA substitutions using first-principles calculations based on virtual-crystal approximation, and a possible high T_c of 280 K was predicted for $H_3S_{0.925}P_{0.075}$ with an $Im\bar{3}m$ structure at 250 GPa [44]. Note that in both Refs. [43,44], all the structures studied were acquired by atomic substitution based on the $Im\bar{3}m$ structure of H_3S, but phase transition is ineluctable when the substitution rate becomes too high. The crystal structure evidently plays an essential role in the superconductivity and can even lead to the metal-semiconductor transition.

This paper reports the effect of covalent bonding on the superconductivity of the hypothetical compound H_6SSe. First-principles structure searches reveal three candidate structures for H_6SSe at 200 GPa. The three structures are based on the cubic $Im\bar{3}m$ H_3S structure with different Se substitutions, which result in different bond strengths of covalent H-S or H-Se bonds. Electron-phonon coupling calculations reveal that all the structures exhibit superconductivity, but T_c decreases with the decreasing strength of the weakest covalent bond in each H_6SSe structure. Oxygen substitution to form H_6SO, however, exhibits a rather different structure with semiconducting properties. We attribute this to the stronger electronegativity of O (3.44) relative to S (2.58) or Se (2.55). Our simulations provide direct evidence for the significance of strong covalent bonding to the high T_c of the H-S-Se system.

II. COMPUTATIONAL DETAILS

The search for crystalline structures is performed using a particle-swarm optimization algorithm, as implemented in the CALYPSO code [45,46]. CALYPSO is one of the most authoritative structure prediction methods in the field and has been successfully used to predict the stable or metastable ground-state structures of various systems at high pressures [14,24,47–50]. Simulation cells up to 4 f.u. for H_6SSe and H_6SO are used in structure predictions at 200 GPa to approximate experimental conditions. Structural relaxations and electronic structure calculations are performed using the projector augmented-wave (PAW) method [51] in the Vienna Ab initio Simulation Package (VASP) [52]. Exchange-correlation potentials are treated within the generalized gradient approximation of Perdew-Burke-Ernzerhof theory [53]. The all-electron PAW method is adopted for O, S, and Se atoms with valence electrons of $2s^2 2p^4$, $3s^2 3p^4$, and $4s^2 4p^4$, respectively. A cutoff energy for the expansion of the wave function into the plane wave basis is set to 1000 eV. Monkhorst-Pack k-point meshes [54] with a grid density of $0.20 Å^{-1}$ are chosen to ensure total energy convergence better than 1 meV per atom. To evaluate the distribution of S and Se in H_6SSe, we have generated various special quasirandom structures (SQSs) [55–57] using the MCSQS code as implemented in the Alloy Theoretic Automated Toolkit (ATAT) [58]. First-principles molecular dynamics (MD) simulations using the canonical NVT (N is the number of particles, V is volume, and T is temperature) are performed with a time step of 1 fs. The temperature was controlled at 300 K with $3 \times 3 \times 3$ supercells (216 atoms), $3 \times 3 \times 2$ supercells (144 atoms), and $2 \times 2 \times 2$ supercells (128 atoms) for the $Pm\bar{3}m$, $Cmmm$, and $Fd\bar{3}m$ phases of H_6SSe, respectively. The phonon spectrum

TABLE I. Optimized structure parameters of the three H_6SSe phases at 200 GPa.

Space group	Lattice parameters (Å)	Volume (Å^3/atom)	Atomic positions
$Pm\bar{3}m$	$a = 3.07$	3.62	S ($1a$) $(0,0,0)$
			Se ($1b$) $(0.5, 0.5, 0.5)$
			H ($3c$) $(0.5, 0, 0.5)$
			H ($3d$) $(0, 0.5, 0)$
$Cmmm$	$a = 4.30$	3.61	S ($2b$) $(0.5, 0, 0)$
	$b = 3.07$		Se ($2d$) $(0, 0, 0.5)$
	$c = 4.37$		H ($2a$) $(0, 0, 0)$
			H ($2c$) $(0.5, 0, 0.5)$
			H ($8o$) $(0.26, 0, 0.23)$
$Fd\bar{3}m$	$a = 6.13$	3.59	S ($8b$) $(0.5, 0.5, 0.5)$
			Se ($8a$) $(0, 0, 0)$
			H ($48f$) $(0.5, 0.5, 0.27)$

and electron-phonon coupling (EPC) of the compounds are calculated within the framework of linear-response theory through the QUANTUM ESPRESSO code [59]. Norm-conserving pseudopotentials for S, Se, and H elements are used with a kinetic cutoff energy of 100 Ry. A q mesh of $10 \times 10 \times 10$ (47 q points) and a k mesh of $40 \times 40 \times 40$ for the $Im\bar{3}m$ phase of H_3S in the first Brillouin zone is used in the EPC calculations. The $8 \times 8 \times 8$ (35 q points), $6 \times 6 \times 6$ (52 q points), and $8 \times 8 \times 8$ (29 q points) q meshes in the first Brillouin zone are used for the $Pm\bar{3}m$, $Cmmm$, and $Fd\bar{3}m$ phases of H_6SSe, respectively. Correspondingly, Monkhorst-Pack grids of $32 \times 32 \times 32$, $24 \times 24 \times 24$, and $32 \times 32 \times 32$ are used to ensure the k-point sampling converges with Gaussians of width 0.04 Ry for the three phases of H_6SSe, respectively.

III. RESULTS AND DISCUSSION

Figure 1 shows the cubic $Im\bar{3}m$ structure of H_3S at 200 GPa. The S atoms locate at a bcc lattice, with each S atom bonded with six H atoms, while H atoms locate symmetrically
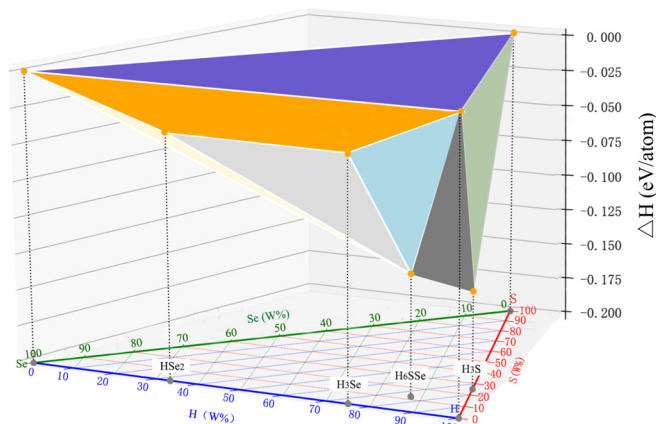

FIG. 2. Predicted formation enthalpy of various H-S-Se compounds with respect to elemental decomposition into H_2, S, and Se at 200 GPa. Compounds corresponding to data points located on the convex hull are energetically stable against decomposition into other compositions.

TABLE II. Formation enthalpies (eV/atom) of H_6SSe at 200 GPa. ΔH_{f1}, ΔH_{f2}, ΔH_{f3}, ΔH_{f4}, ΔH_{f5}, and ΔH_{f6} represent the decomposition of H_6SSe into $H_3S + H_3Se$, $H_3S + 3/2H_2 + Se$, $1/2HSe_2 + H_3S + 5/4H_2$, $3/2H_2 + S + H_3Se$, $3H_2 + S + Se$, and $S + 11/4H_2 + 1/2HSe_2$, respectively. The $Im\bar{3}m$ structures of H_3S [27] and H_3Se [60], the $Im\bar{3}m$ structure of Se [61], the $C2/m$ structure of HSe_2 [60], and the $Cmca$ structure of H_2S [24] are adopted in the calculations.

	ΔH_{f1}	ΔH_{f2}	ΔH_{f3}	ΔH_{f4}	ΔH_{f5}	ΔH_{f6}
$Pm\bar{3}m$	0.024	0.006	0.013	−0.043	−0.060	−0.054
$Cmmm$	−0.003	−0.021	−0.015	−0.071	−0.088	−0.082
$Fd\bar{3}m$	−0.032	−0.050	−0.044	−0.100	−0.117	−0.111

between two neighboring S atoms. Therefore, this structure can be viewed as two interlaced identical simple cubic H_3S sublattices, as shown in the right panel of Fig. 1(a). For H_6SSe at 200 GPa, three structures with similar enthalpies were predicted with space groups $Pm\bar{3}m$, $Cmmm$, and $Fd\bar{3}m$, as shown in Figs. 1(b), 1(c) and 1(d), respectively. Of note, they keep the main framework of the cubic $Im\bar{3}m$ structure of H_3S, which means they can be obtained from $Im\bar{3}m$ H_3S with half its S atoms substituted by Se atoms. For example, the $Pm\bar{3}m$ structure of H_6SSe can be viewed as the body-centered S atoms in $Im\bar{3}m$ H_3S substituted by Se atoms, forming two simple cubic sublattices of H_3S and H_3Se, as shown in the right panels of Fig. 1. The $Cmmm$ and $Fd\bar{3}m$ structures have half the S atoms in a cubic sublattice in H_3S replaced by Se atoms, i.e., those siting on a diagonal plane and at the vertices of a tetrahedron, respectively. In fact, the structure searches also predict several other structures with different Se substitutions, but with much higher enthalpies ($\geqslant 0.56$ eV per H_6SSe f.u.) compared to these three structures. Therefore, we did not consider these structures in our study. The optimized structural parameters of the three predicted H_6SSe structures at 200 GPa are summarized in Table I.

We further study the thermodynamic stability of the H-S-Se system by calculating the formation enthalpies ΔH with respect to mixtures of elemental H_2, S, and Se at 200 GPa. Figure 2 summarizes the formation enthalpies of the considered compounds normalized on a per atom basis for the most energetically favorable structures. The phases lying on the convex hull are thermodynamically stable against decomposition into other compositions. H_2S was found to dissociate into H_3S and S, which is consistent with previous studies [26–29]. We thus did not include H_2S in Fig. 2. Moreover, it is obvious that H_6SSe is thermodynamically stable against decomposition into other compositions.

Figure 2 also provides six candidate routes to synthesize H_6SSe, namely, compressing mixtures of $H_3S + H_3Se$, $H_3S + H_2 + Se$, $HSe_2 + H_3S + H_2$, $H_2 + S + H_3Se$, $H_2 + S + Se$, or $S + H_2 + HSe_2$. Table II summarizes the formation enthalpies of H_6SSe related to the six possible routes. Significantly, the most energetically stable $Fd\bar{3}m$ structure always possesses negative formation enthalpies. The effect of vibrational entropy on the formation energy of H_6SSe was also considered within the quasiharmonic approximation [62]. Here, only the decomposition path to H_3S and H_3Se was considered since it has the highest formation enthalpy
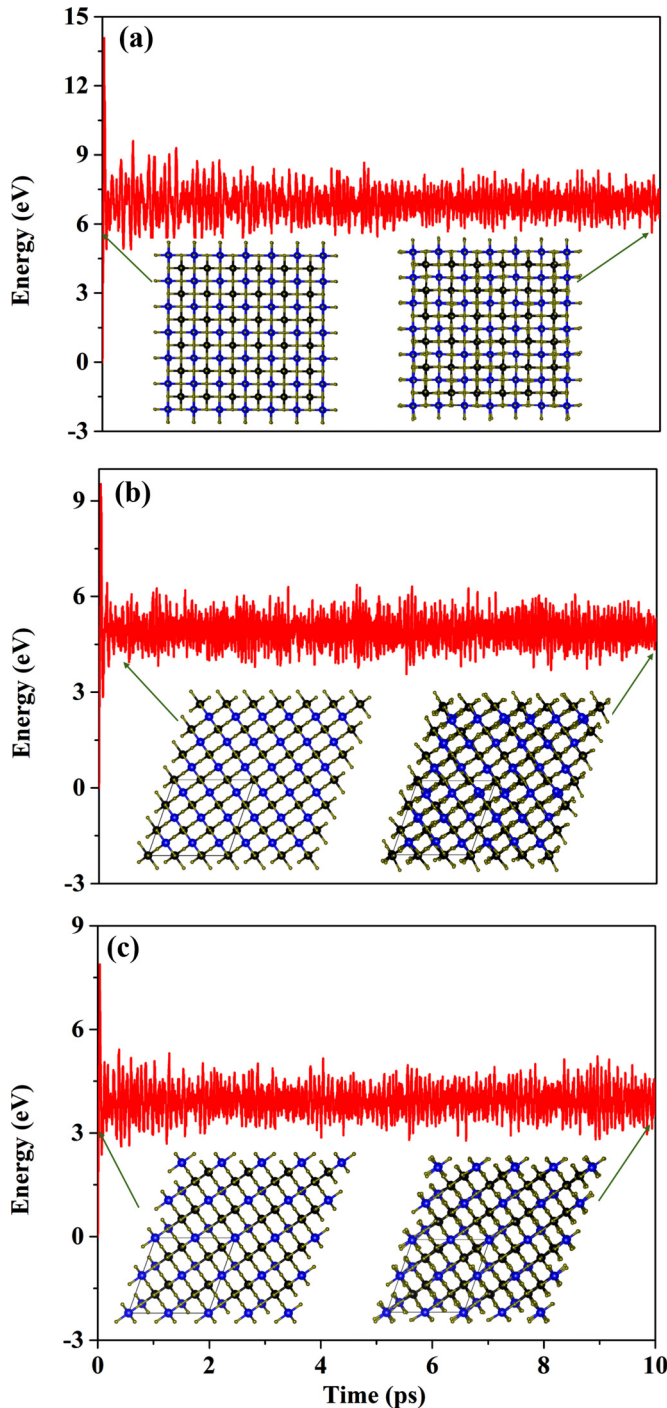
FIG. 3. Evolution of relative enthalpies during molecular dynamics simulation starting from (a) the $Pm\bar{3}m$, (b) the $Cmmm$, and (c) the $Fd\bar{3}m$ structures of H_6SSe at 200 GPa, $T = 300$ K. The insets are snapshots of structures at the start and end of 10-ps simulations, respectively.

of -0.032 eV/atom at 0 K. Interestingly, the formation energy of H_6SSe remains negative (-0.049 eV/atom) with the inclusion of vibrational entropy up to 300 K, implying that H_6SSe is thermodynamically stable against decomposition at least up to 300 K. Furthermore, we performed the NVT-MD simulations to examine the thermal stability of the three structures of
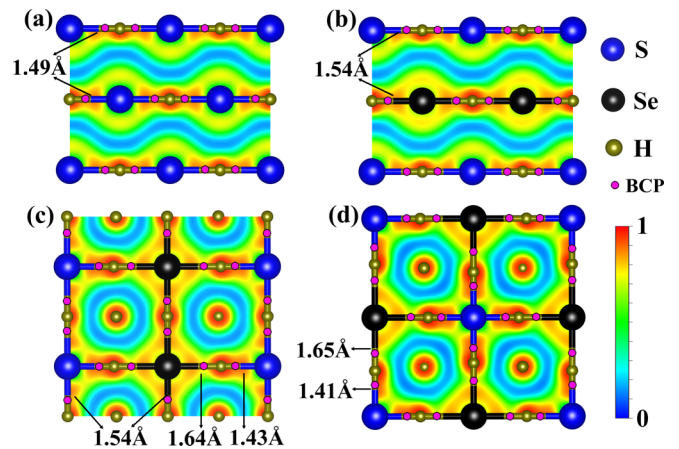

FIG. 4. Two-dimensional valence electron localization functions of (a) the $Im\bar{3}m$ structure of H_3S and the (b) $Pm\bar{3}m$, (c) $Cmmm$, and (d) $Fd\bar{3}m$ structures of H_6SSe at 200 GPa in planes containing H-S and H-Se bonds. The pink dots correspond to the bond critical points (BCPs).

H_6SSe compounds at 200 GPa and $T = 300$ K. As shown in Fig. 3, no structural collapse was observed after 10 ps (10 000 steps), indicating the thermal stability of H_6SSe.

The disorder effect of H_6SSe was examined by performing SQS calculations. Various SQS-N structures (with $N = 8$, 16, 24, and 32 atoms per unit cell) were generated for the random bcc alloys $H_3S_xSe_{1-x}$ at composition $x = 0.5$. After full optimization, we found the most stable structure (SQS-16) possesses higher energy (70 meV/f.u. at 0 K and 73 meV/f.u. at 300 K within the quasiharmonic approximation [62]) than our predicted $Fd\bar{3}m$ structure, indicating that H_6SSe is an ordered phase.

Figure 4 shows the electron localization function (ELF) [63] of different structures of H_3S and H_6SSe to explore the effect of different Se substitutions on the strength of the covalent bonds. The ELF is developed in quantum chemistry to visualize covalent bonds and lone pairs, and it maps values in the range from 0 to 1, with 1 corresponding to perfect localization of valence electrons, implying a strong covalent bond. In the $Im\bar{3}m$ structure of H_3S, all H-S bonds have a length of 1.49 Å, with a maximum ELF of ~0.9 at 200 GPa [Fig. 4(a)], indicating their relatively strong covalent nature, which agrees well with previous work [27]. The $Pm\bar{3}m$ structure of H_6SSe consists of two interlaced cubic H_3S and H_3Se sublattices, with each H atom bonded only to two neighboring S or Se atoms, resulting in H-S and H-Se having the same bond lengths. However, the larger atomic radius of Se induces longer H-S and H-Se bond lengths (1.54 Å), resulting in weaker covalent bonding in $Pm\bar{3}m$ H_6SSe than in $Im\bar{3}m$ H_3S. In the $Cmmm$ structure, half the H atoms are shared by S and Se atoms, resulting in two different bond lengths each for H-S (1.43 and 1.54 Å) and H-Se (1.64 and 1.54 Å). Therefore, ELF calculations reveal obviously weaker H-Se bonds in the $Cmmm$ structure. In the $Fd\bar{3}m$ structure, all H atoms are shared by S and Se atoms, with H-S and H-Se bond lengths of 1.41 and 1.65 Å, respectively. Note that the H-S bonds in the $Cmmm$ and $Fd\bar{3}m$ structures are even shorter than those in $Im\bar{3}m$-H_3S, which is understandable

TABLE III. Topological analysis of covalent bonding, the electron-phonon coupling constant λ, the logarithmically averaged phonon frequency ω_{log}, and the resultant T_c of H_3S and H_6SSe at 200 GPa.

Phases	H-S bond		H-Se bond		λ	ω_{log} (K)	T_c (K)
	d (Å)	$\nabla^2\rho(r)\,(e^-\,\text{Å}^{-5})$	d (Å)	$\nabla^2\rho(r)\,(e^-\,\text{Å}^{-5})$			
$Im\bar{3}m$ H_3S	1.49	-5.0933			1.87	1337	246
$Pm\bar{3}m$ H_6SSe	1.54	-3.9563	1.54	-4.0425	1.76	1125	196
$Cmmm$ H_6SSe	1.43	-8.4826	1.64	-1.4108	1.60	1137	181
	1.54	-4.1242	1.54	-3.7367			
$Fd\bar{3}m$ H_6SSe	1.41	-9.467	1.65	-0.9499	0.99	1372	115

considering the slightly higher electronegativity of S (2.58) compared with Se (2.55). Note that any decrease in H-S bond length is always accompanied by an increase in H-Se bond length.

Further topological analysis of the all-electron charge density of H_3S and H_6SSe is conducted using the quantum theory of atoms in molecules [64]. In this theory, a solid is defined as a zero-flux surface of the electron density gradient $\nabla\rho(r)$. The charge density distribution $\rho(r)$ and its principal curvatures (three eigenvalues of the Hessian matrix) at the bond critical point reveal information about the type and properties of bonding (see pink dots in Fig. 4). The sign of the Laplacian of the electron density $\nabla^2\rho(r)$ indicates whether the density is locally concentrated (negative) or depleted (positive). The resultant Laplacian $\nabla^2\rho(r)$ values of different H-S and H-Se bonds are listed in Table III. As expected, all the values for these bonds in H_3S and H_6SSe are negative, indicating obviously covalent interactions between H and Se (or S) atoms. Previous work has shown that $\nabla^2\rho(r)$ values at critical points can efficiently reflect the strength of heteronuclear covalent

bonds [65,66], especially for covalent hydrides [67]. The covalent H-S and H-Se bonds show two different strength trends. Compared with $Im\bar{3}m$ H_3S, the strength of the strongest H-S bonds decreases in the $Pm\bar{3}m$ structure but increases in the $Cmmm$ and $Fd\bar{3}m$ structures. However, the strength of H-Se bonds decreases from the $Pm\bar{3}m$ to the $Cmmm$ and $Fd\bar{3}m$ structures, consistent with the ELF calculation results.

Calculated electronic band structures and partial electronic densities of states (DOSs) for the three structures of H_6SSe and the $Im\bar{3}m$ structure of H_3S at 200 GPa further explore their electronic properties, as shown in Fig. 5. Like the $Im\bar{3}m$ structure of H_3S (Fig. 5), all three structures of H_6SSe exhibit metallic features with bands crossing the Fermi level. The coexistence of steep and flat bands crossing the Fermi energy level indicates their possible superconductivity. Specifically, the electronic band dispersions of $Im\bar{3}m$ H_3S and $Pm\bar{3}m$ H_6SSe are barely distinguishable, with only two degenerate bands along the X-R-M directions, similar to previous observations for H_3S and H_3Se [60]. The calculated total DOS at the Fermi level decreased in H_6SSe, namely,
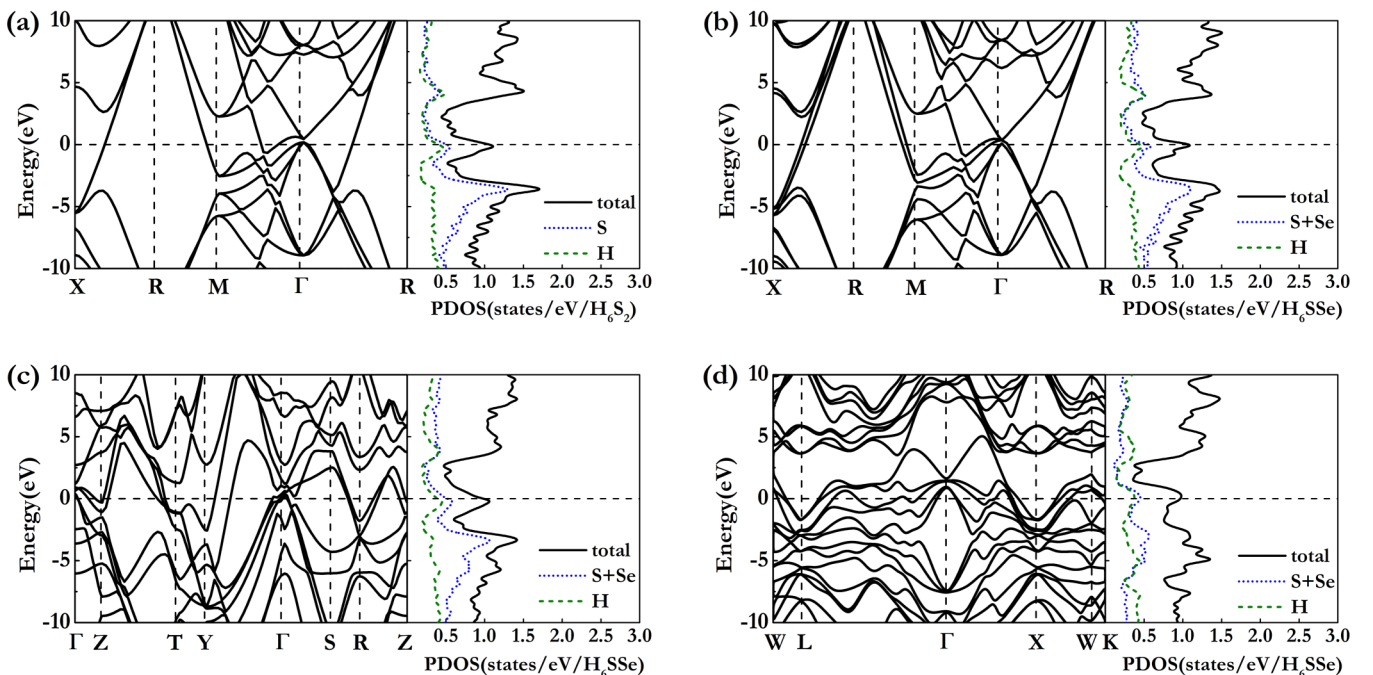

FIG. 5. Electronic band structure and partial electronic density of states (PDOS) of (a) the $Im\bar{3}m$ structure of H_3S and the (b) $Pm\bar{3}m$, (c) $Cmmm$, and (d) $Fd\bar{3}m$ structures of H_6SSe at 200 GPa.
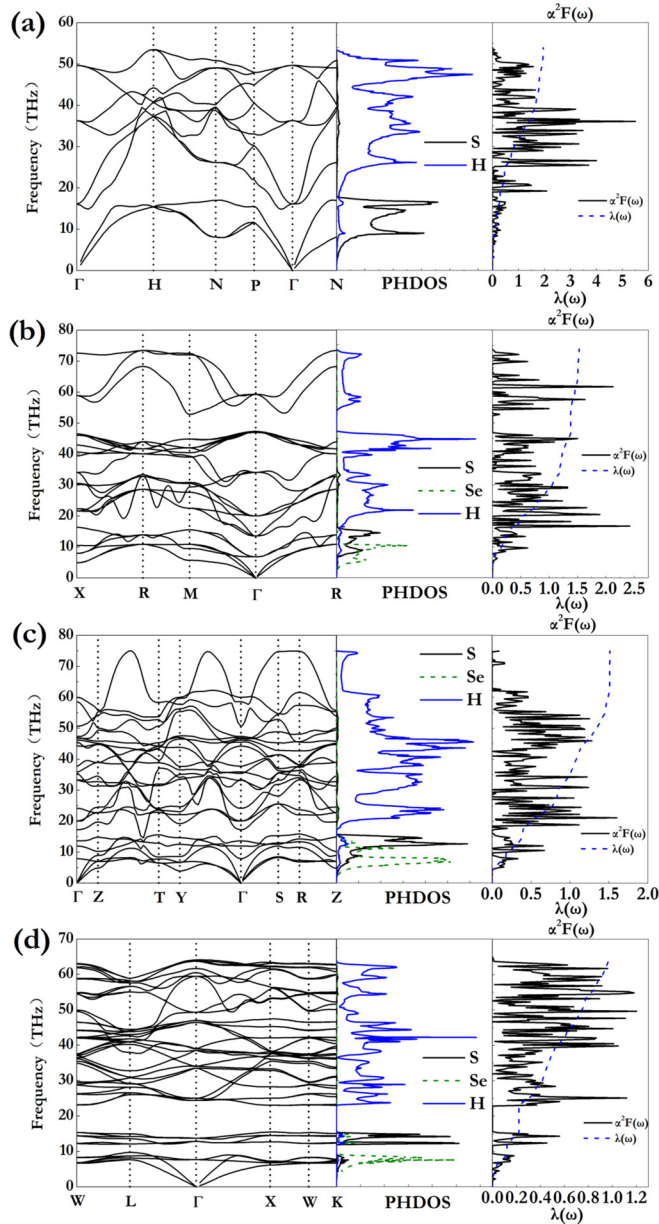
FIG. 6. Phonon dispersions, projected phonon density of states (PHDOS), Eliashberg spectral function $\alpha^2 F(\omega)$, and EPC integration of $\lambda(\omega)$ of (a) the $Im\bar{3}m$ structure of H_3S and the (b) $Pm\bar{3}m$, (c) $Cmmm$, and (d) $Fd\bar{3}m$ structures of H_6SSe at 200 GPa.

0.13, 0.12, and 0.11 eV^{-1} per atom for $Pm\bar{3}m$, $Cmmm$, and $Fd\bar{3}m$, respectively, which is less than or equal to that of H_3S (0.13 eV^{-1} per atom), possibly indicating decreasing T_c values. For H_3S [Fig. 5(a)], strong H-S hybridization can be derived from the significant overlap of H and S DOS profiles and has been demonstrated to be responsible for its high superconductivity. Moreover, H-derived states around the Fermi level exhibit strong structural independence; however, the projected DOSs from the sum of S and Se atoms change slightly in different structures, especially in the $Fd\bar{3}m$ structure, showing an obvious decrease of states around the Fermi energy.

Figure 6 presents the phonon dispersions, projected phonon density of states, Eliashberg spectral function $\alpha^2F(\omega)$,
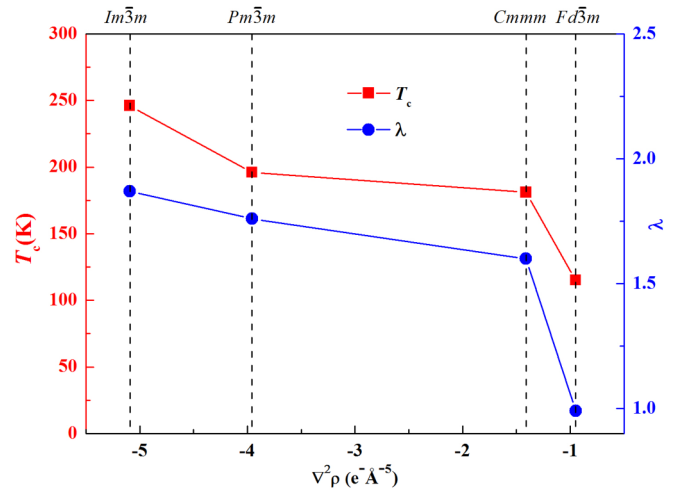

FIG. 7. Evolution of T_c and electron-phonon coupling constant λ as a function of bond strength of the weakest covalent bonds in H_3S and H_6SSe.

and EPC integrated $\lambda(\omega)$ of H_3S and H_6SSe at 200 GPa. Dynamical stability is clearly evidenced by the absence of imaginary frequencies in the whole Brillouin zone for the three predicted structures of H_6SSe. As expected, the vibrational modes are divided into two parts, with low translational frequencies dominated by S/Se atoms and the high ends related to H atoms. Unlike the electronic bands, phonons strongly depend on the material and structure. The $Pm\bar{3}m$ structure shows a clear "gap" between the high-frequency (>50 THz) H-stretching vibrations and the midfrequency (20–50 THz) H-wagging and bending modes, similar to H_3Se [60]. The $Cmmm$ structure is much more complicated, with mixed H-derived vibrational modes, while the $Fd\bar{3}m$ structure shows easily distinguished vibrational mode subsets for H, S, and Se with obvious intervals. The superconducting T_c was estimated from the spectral function $\alpha^2 F(\omega)$ by numerically solving the Eliashberg equations [68] with a typical choice of Coulomb pseudopotential $\mu^* = 0.1$. Coulomb repulsion is considered in terms of μ^* scaled to a cutoff frequency [69]. The calculated EPC parameters λ for $Im\bar{3}m$, $Pm\bar{3}m$, $Cmmm$, and $Fd\bar{3}m$ at 200 GPa are 1.87, 1.76, 1.60, and 0.99, leading to decreasing values of T_c of 246, 196, 181, and 115 K, respectively.

We investigate the effect of covalent bonding on the high-T_c chalcogen hydrides in Table III, showing T_c to depend on the Laplacian $\nabla^2\rho$. Note that the EPC constant λ and T_c of H_3S and H_6SSe are closely related to the weakest covalent bonds in the structures. As shown in Fig. 7, λ decreases with decreasing strength of the weakest covalent bonds, first gradually from 1.87 in $Im\bar{3}m$ H_3S to 1.60 in $Pm\bar{3}m$ H_6SSe and then sharply to 0.99 in $Fd\bar{3}m$ H_6SSe. The values of T_c show corresponding decreases from 246 to 181 K and then to 115 K. These results highlight the key role of strong covalent bonding in improving the T_c of hydrogen-containing superconductors.

We also investigate O substitution for comparison, namely, H_6SO with a predicted $P\bar{1}$ structure that no longer keeps the original cubic framework of H_3S. Instead, it contains H_4S and H_4O units and isolated "H_2" units with bond lengths of
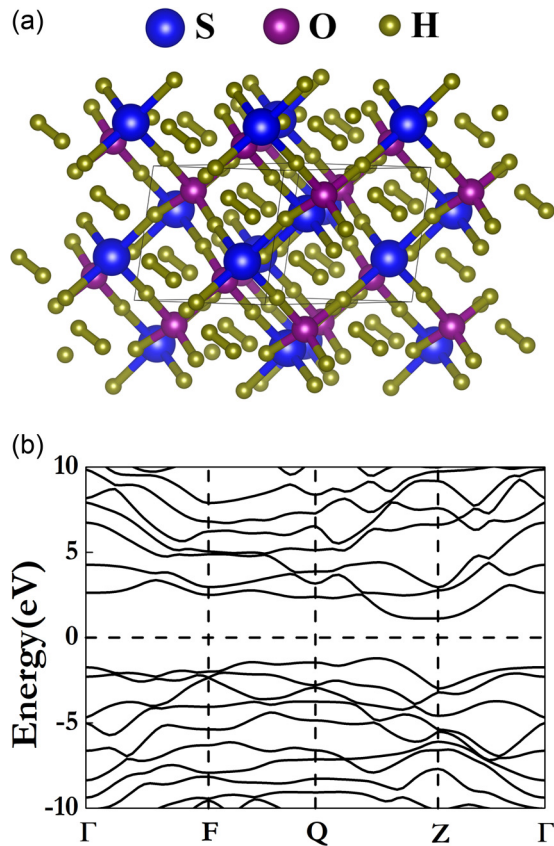
FIG. 8. (a) Crystal structure and (b) electronic band structures for the $P\bar{1}$ structure of H_6SO at 200 GPa.

0.73 Å at 200 GPa, as shown in Fig. 8. The electronic band structure [Fig. 8(b)] shows the $P\bar{1}$ structure of H_6SO is a semiconductor with an indirect band gap of 2.32 eV. Thus, this compound is not considered further. We attribute the difference between H_6SSe and H_6SO to the different Pauling electronegativities of O and Se. Given the similar electronegativities of Se (2.55) and S (2.58), Se substitution keeps the original cubic framework of H_3S. However, their group neighbor O has a much larger electronegativity of 3.44 that breaks the cubic structure of H_3S and leads to the formation of a semiconducting phase with isolated H_2 units. It should be noted that the current results violate the earlier proposal that H_6SO is a superconductor with T_c of ~ 160 K [43,44]. This

is understandable since the previous calculations were based simply on the cubic H_3S structure with half of S substituted by O, which is energetically much higher (2.965 eV per H_6SO f.u.) than our predicted $P\bar{1}$ structure. Therefore, our results also highlight the necessity of performing thorough structure prediction in order to investigate accurately the physical properties of new materials.

IV. CONCLUSIONS

In summary, we studied systematically the influence of covalent bonding on the superconductivity of H_3S by replacing half the S with Se to construct hypothetical H_6SSe. Combining atom substitutions with global-minimum structure searching, we identified three dynamically stable structures for H_6SSe at 200 GPa with space groups $Pm\bar{3}m$, $Cmmm$, and $Fd\bar{3}m$. The three structures retain the main features of the cubic $Im\bar{3}m$ phase of H_3S, with only different Se substituting positions. We demonstrated that the T_c of the H_6SSe compounds decreases with the decreasing strength of the weakest covalent bond in the structures, suggesting the key role of covalent bonds in determining the T_c of the H-S-Se system. Oxygen substitution, however, led to a very different structure (H_6SO), showing semiconducting properties. We attribute this difference to O having a larger Pauling electronegativity than S or Se. Our results imply that the pursuit of potential high-T_c superconductors must carefully consider the strength of covalent bonding.

[1] D. Van Delft and P. Kes, Phys. Today **63**(9), 38 (2010).

[2] J. Bardeen, L. N. Cooper, and J. R. Schrieffer, Phys. Rev. **108**, 1175 (1957).

[3] N. W. Ashcroft, Phys. Rev. Lett. **21**, 1748 (1968).

[4] R. P. Dias and I. F. Silvera, Science **355**, 715 (2017).

[5] N. W. Ashcroft, Phys. Rev. Lett. **92**, 187002 (2004).

[6] W. Cui, J. Shi, H. Liu, Y. Yao, H. Wang, T. Iitaka, and Y. Ma, Sci. Rep. **5**, 13039 (2015).

[7] D. Y. Kim, R. H. Scheicher, S. Lebègue, J. Prasongkit, B. Arnaud, M. Alouani, and R. Ahuja, Proc. Natl. Acad. Sci. USA **105**, 16454 (2008).

[8] Y. Yao, J. Tse, Y. Ma, and K. Tanaka, Europhys. Lett. **78**, 37003 (2007).

[9] M. Martinez-Canales, A. R. Oganov, Y. Ma, Y. Yan, A. O. Lyakhov, and A. Bergara, Phys. Rev. Lett. **102**, 087005 (2009).

[10] X. Jin, X. Meng, Z. He, Y. Ma, B. Liu, T. Cui, G. Zou, and H.-k. Mao, Proc. Natl. Acad. Sci. USA **107**, 9969 (2010).

[11] J. A. Flores-Livas, M. Amsler, T. J. Lenosky, L. Lehtovaara, S. Botti, M. A. L. Marques, and S. Goedecker, Phys. Rev. Lett. **108**, 117004 (2012).

[12] G. Gao, A. R. Oganov, A. Bergara, M. Martinez-Canales, T. Cui, T. Iitaka, Y. Ma, and G. Zou, Phys. Rev. Lett. **101**, 107002 (2008).

[13] Y. Yao and D. D. Klug, Proc. Natl. Acad. Sci. USA **107**, 20893 (2010).

[14] Y. Li, G. Gao, Y. Xie, Y. Ma, T. Cui, and G. Zou, Proc. Natl. Acad. Sci. USA **107**, 15708 (2010).

[15] J. A. Flores-Livas, M. Amsler, C. Heil, A. Sanna, L. Boeri, G. Profeta, C. Wolverton, S. Goedecker, and E. K. U. Gross, Phys. Rev. B **93**, 020508 (2016).

[16] A. Shamp, T. Terpstra, T. Bi, Z. Falls, P. Avery, and E. Zurek, J. Am. Chem. Soc. **138**, 1884 (2015).

[17] H. Liu, Y. Li, G. Gao, J. S. Tse, and I. I. Naumov, J. Phys. Chem. C **120**, 3458 (2016).

[18] Y. Fu, X. Du, L. Zhang, F. Peng, M. Zhang, C. J. Pickard, R. J. Needs, D. J. Singh, W. Zheng, and Y. Ma, Chem. Mater. **28**, 1746 (2016).

[19] H. Wang, S. T. John, K. Tanaka, T. Iitaka, and Y. Ma, Proc. Natl. Acad. Sci. USA **109**, 6463 (2012).

[20] Y. Li, J. Hao, H. Liu, S. T. John, Y. Wang, and Y. Ma, Sci. Rep. **5**, 9948 (2015).

[21] H. Liu, I. I. Naumov, R. Hoffmann, N. Ashcroft, and R. J. Hemley, Proc. Natl. Acad. Sci. USA **114**, 6990 (2017).

[22] F. Peng, Y. Sun, C. J. Pickard, R. J. Needs, Q. Wu, and Y. Ma, Phys. Rev. Lett. **119**, 107001 (2017).

[23] A. Drozdov, M. Eremets, I. Troyan, V. Ksenofontov, and S. Shylin, Nature (London) **525**, 73 (2015).

[24] Y. Li, J. Hao, H. Liu, Y. Li, and Y. Ma, J. Chem. Phys. **140**, 174712 (2014).

[25] I. Troyan, A. Gavriliuk, R. Rüffer, A. Chumakov, A. Mironovich, I. Lyubutin, D. Perekalin, A. P. Drozdov, and M. I. Eremets, Science **351**, 1303 (2016).

[26] I. Errea, M. Calandra, C. J. Pickard, J. Nelson, R. J. Needs, Y. Li, H. Liu, Y. Zhang, Y. Ma, and F. Mauri, Phys. Rev. Lett. **114**, 157004 (2015).

[27] D. Duan, Y. Liu, F. Tian, D. Li, X. Huang, Z. Zhao, H. Yu, B. Liu, W. Tian, and T. Cui, Sci. Rep. **4**, 6968 (2014).

[28] I. Errea, M. Calandra, C. J. Pickard, J. R. Nelson, R. J. Needs, Y. Li, H. Liu, Y. Zhang, Y. Ma, and F. Mauri, Nature (London) **532**, 81 (2016).

[29] Y. Li, L. Wang, H. Liu, Y. Zhang, J. Hao, C. J. Pickard, J. R. Nelson, R. J. Needs, W. Li, Y. Huang *et al.*, Phys. Rev. B **93**, 020103 (2016).

[30] T. Ishikawa, A. Nakanishi, K. Shimizu, H. Katayama-Yoshida, T. Oda, and N. Suzuki, Sci. Rep. **6**, 23160 (2016).

[31] R. Akashi, W. Sano, R. Arita, and S. Tsuneyuki, Phys. Rev. Lett. **117**, 075503 (2016).

[32] I. Kruglov, R. Akashi, S. Yoshikawa, A. R. Oganov, and M. M. D. Esfahani, Phys. Rev. B **96**, 220101 (2017).

[33] M. Einaga, M. Sakata, T. Ishikawa, K. Shimizu, M. I. Eremets, A. P. Drozdov, I. A. Troyan, N. Hirao, and Y. Ohishi, Nat. Phys. **12**, 835 (2016).

[34] F. Capitani, B. Langerome, J.-B. Brubach, P. Roy, A. Drozdov, M. Eremets, E. Nicol, J. Carbotte, and T. Timusk, Nat. Phys. **13**, 859 (2017).

[35] A. P. Durajski, R. Szczęśniak, and Y. Li, Physica C **515**, 1 (2015).

[36] N. Bernstein, C. S. Hellberg, M. D. Johannes, I. I. Mazin, and M. J. Mehl, Phys. Rev. B **91**, 060511(R) (2015).

[37] A. Majumdar, J. S. Tse, and Y. Yao, Angew. Chem., Int. Ed **129**, 11548 (2017).

[38] Y. Yao and J. S. Tse, Chem. - Eur. J. **24**, 1769 (2018).

[39] T. A. Strobel, P. Ganesh, M. Somayazulu, P. R. C. Kent, and R. J. Hemley, Phys. Rev. Lett. **107**, 255503 (2011).

[40] M. Komelj and H. Krakauer, Phys. Rev. B **92**, 205125 (2015).

[41] W. Sano, T. Koretsune, T. Tadano, R. Akashi, and R. Arita, Phys. Rev. B **93**, 094525 (2016).

[42] Y. Quan and W. E. Pickett, Phys. Rev. B **93**, 104526 (2016).

[43] C. Heil and L. Boeri, Phys. Rev. B **92**, 060508 (2015).

[44] Y. Ge, F. Zhang, and Y. Yao, Phys. Rev. B **93**, 224513 (2016).

[45] Y. Wang, J. Lv, L. Zhu, and Y. Ma, Phys. Rev. B **82**, 094116 (2010).

[46] Y. Wang, J. Lv, L. Zhu, and Y. Ma, Comput. Phys. Commun. **183**, 2063 (2012).

[47] J. Shi, W. Cui, S. Botti, and M. A. Marques, Phys. Rev. Mater. **2**, 023604 (2018).

[48] L. Zhu, H. Liu, C. J. Pickard, G. Zou, and Y. Ma, Nat. Chem. **6**, 644 (2014).

[49] J. Lv, Y. Wang, L. Zhu, and Y. Ma, Phys. Rev. Lett. **106**, 015503 (2011).

[50] L. Zhu, H. Wang, Y. Wang, J. Lv, Y. Ma, Q. Cui, Y. Ma, and G. Zou, Phys. Rev. Lett. **106**, 145501 (2011).

[51] G. Kresse and D. Joubert, Phys. Rev. B **59**, 1758 (1999).

[52] G. Kresse and J. Furthmüller, Phys. Rev. B **54**, 11169 (1996).

[53] J. P. Perdew, K. Burke, and M. Ernzerhof, Phys. Rev. Lett. **77**, 3865 (1996).

[54] H. J. Monkhorst and J. D. Pack, Phys. Rev. B **13**, 5188 (1976).

[55] A. Zunger, S.-H. Wei, L. G. Ferreira, and J. E. Bernard, Phys. Rev. Lett. **65**, 353 (1990).

[56] K. C. Hass, L. C. Davis, and A. Zunger, Phys. Rev. B **42**, 3757(R) (1990).

[57] S.-H. Wei, L. G. Ferreira, J. E. Bernard, and A. Zunger, Phys. Rev. B **42**, 9622 (1990).

[58] A. Van de Walle, P. Tiwary, M. De Jong, D. Olmsted, M. Asta, A. Dick, D. Shin, Y. Wang, L.-Q. Chen, and Z.-K. Liu, Calphad **42**, 13 (2013).

[59] P. Giannozzi, J. Phys.: Condens. Matter **21**, 395502 (2009).

[60] S. Zhang, Y. Wang, J. Zhang, H. Liu, X. Zhong, H.-F. Song, G. Yang, L. Zhang, and Y. Ma, Sci. Rep. **5**, 15433 (2015).

[61] M. I. McMahon, C. Hejny, J. S. Loveday, L. F. Lundegaard, and M. Hanfland, Phys. Rev. B **70**, 054101 (2004).

[62] P. Pavone, S. Baroni, and S. de Gironcoli, Phys. Rev. B **57**, 10421 (1998).

[63] A. D. Becke and K. E. Edgecombe, J. Chem. Phys. **92**, 5397 (1990).

[64] C. Katan, P. Rabiller, C. Lecomte, M. Guezo, V. Oison, and M. Souhassou, J. Appl. Crystallogr. **36**, 65 (2003).

[65] Y. Li, X. Feng, H. Liu, J. Hao, S. A. Redfern, W. Lei, D. Liu, and Y. Ma, Nat. Commun. **9**, 722 (2018).

[66] H. Liu, Y. Yao, and D. D. Klug, Phys. Rev. B **91**, 014102 (2015).

[67] S. Shaik, D. Danovich, B. Braida, W. Wu, and P. C. Hiberty, in *The Chemical Bond II: 100 Years Old and Getting Stronger*, edited by D. M. P. Mingos (Springer, Cham, 2016), pp. 169–211.

[68] G. Eliashberg, Sov. Phys. JETP **11**, 696 (1960).

[69] Y. Yao, J. S. Tse, K. Tanaka, F. Marsiglio, and Y. Ma, Phys. Rev. B **79**, 054524 (2009).